Numerical analysis of the phased array imaging with a stacked plate buffer

Mingqian Xia, Takahiro Hayashi*, and Naoki Mori

Department of Mechanical Engineering, Graduate School of Engineering, Osaka University

E-mail: hayashi@mech.eng.osaka-u.ac.jp

This paper discusses the imaging with a phased array transducer attached with a stacked thin plate buffer using the calculations of wave propagation. The buffer is designed to guarantee the performance of phased array transducer based on the properties of dispersion nature of the S0 mode of Lamb wave. First, numerical analyses showed the limitations of the imaging with a stacked plate buffer due to the multiple reflections at the buffer ends. Then the effective detecting region (EDR) of the phased array transducer with a stacked plate buffer was investigated theoretically and numerically. The imaging results of the numerical calculations agreed with the theoretical predictions on the EDR. Final numerical analyses also presented the longer buffer provides the wider EDR as predicted by the theoretical investigations.

1. Introduction

Pipe welds in factories and plants are affected by heat due to welding, and various stress changes and environmental changes in pipes occur during long-term use. Therefore, stress corrosion cracking and fatigue cracking are likely to occur in the heat-affected zone, which is the most important area for the maintenance of piping[1-10]. Especially in nuclear power plants, accurate sizing of cracks in the heat-affected zone is of great interest because it enables accurate decision of pipe-replacement schedule, resulting in reducing radioactive waste and ensuring the integrity of the plant at the same time[11-13].

Imaging techniques using phased-array ultrasound have been used for crack sizing in the heat-affected zone. Phased array ultrasonics is a technique for imaging the source of ultrasonic reflections inside a material by using a large number of signals emitted and detected separately from multiple vibrating elements. The beam forming and focusing are possible by adjusting the delay given to the vibrating elements, and new technologies have also been developed, such as a full matrix capture (FMC), which collects a very large number of waveforms by switching the vibrating elements, and a total focusing method (TFM), which is the imaging algorithm using the large number of waveforms collected by the FMC[14-22].

However, when considering the installation of a phased array probe in plant piping to monitor crack propagation during operation, the high temperature resistance of the phased array probes becomes important when the piping is subjected to high temperatures. For example, in new nuclear power plants that use liquid sodium as a coolant, the temperature of the piping can reach several hundred degrees Celsius, while a typical phased array probe can only maintain its functionality up to about 60 °C.

Buffer rods are often used for ultrasonic measurements at such high temperatures[23, 24]. The buffer rod is a rod-like material coupling an ultrasonic probe with a hot object. It transmits ultrasonic waves, and the rod is cooled by water or air cooling to keep the contact area with the ultrasonic probe below a temperature that the probe can withstand. Usually, a single ultrasonic probe is attached to the end of the rod and the buffer rod has never been used in phased array probes. The main reason is that ultrasonic propagation, such as focusing and beamforming by phased array, is only effective within the near acoustic field and cannot be realized in the far field including buffer rods. This is well known in optics as the diffraction limit[25, 26].

Meanwhile, Fukuchi et al. showed by numerical analysis that ultrasonic focusing in a material beyond the diffraction limit is possible using a buffer consisting of stacked thin

plates[27]. Our recent study presented that the multiple reflections at the buffer ends affects the phased array imaging[28].

In the present study, the characteristics of defect imaging in the material are numerically analyzed considering the features of the thin plate buffer. First, an overview of PA imaging using a thin plate buffer is described, and the characteristics that differ from those of conventional PA imaging are presented. Finally, the theory of effective detective region is confirmed and discussed using numerical calculations.

2. Overview of the phased array imaging using a stacked plate buffer

Ultrasonic phased array imaging is a technique for acquiring images of reflection sources within an object by controlling the delay of each vibrating element of a phased array transducer and matching the phase of the received waveform with a delay calculated from the ultrasonic wave path. Fukuchi et al. showed that ultrasonic wave propagation can be controlled by attaching a thin plate buffer to the phased array transducer[27]. Here, the imaging of the reflection source is discussed.

Figure 1 shows the group velocity dispersion curves of the aluminum alloy plate having the longitudinal and transvers wave velocities of 6400 m/s and 3170 m/s, respectively. The horizontal axis represents the product of the frequency (f) and the thickness (d). The mode structures of fundamental order symmetric (S0) and antisymmetric (A0) modes at 1 MHz mm are also shown. In the low fd range, dispersion nature of the S0 mode is relatively small, which leads the effect that ultrasonic pulse signal maintains its waveform in the buffer plate. Also, the S0 mode in the low fd range has a longitudinal vibration parallel to the longitudinal axis direction, while the A0 mode has a bending vibration in the vertical direction. This indicates that only the S0 mode is efficiently excited when a phased array transducer, which excites longitudinal waves from each element, is in contact with the plate end.

The S0 mode in this low fd range propagates in the stack plate buffer and PA imaging is attempted in this study. Figure 2 shows the calculation model used here, which assumes that the stacked plate buffer is attached to the phased array transducer with 16 elements of 1 MHz center frequency and contacts with a specimen at the other plate-end. The longitudinal force from the phased array transducer is applied at the end of plate.

The calculations of two-dimensional wave propagation were conducted under the conditions of plane strain with COMSOL Multiphysics®. The phased array transducer is

assumed to be a 16-element linear array transducer, and the thin plates with the identical thickness are lined up and are perfectly contacting to the vibration elements. The width of each channel is 0.9 mm and the gap between the elements is 0.1 mm. For all the thin plates in the stacked plate buffer, the left and right surfaces are under traction free boundary condition. From the phased array transducer, vertical dynamic normal force is applied to the upper end of each plate with a center frequency of 1 MHz. The S0 mode of Lamb wave propagating through the stacked plate buffer is transmitted into the specimen. The specimen is perfectly contacted with the lower end of the buffer. The absorption region is attached to the left, right and lower edge of the specimen and suppress all the waves pass through the boundaries of the specimen and absorption region. In this way, the specimen can be assumed to be large enough. Two circular hole defects with 3 mm diameter are on the specimen in the first calculation. The center of the bottom of the stacked plate region is defined as the origin of the xy coordinates, and the positions of the defects are expressed as (x, y). The positions of Defect 1 and Defect 2 are (-10 mm, 20 mm) and (5 mm, 30 mm), respectively.

In these calculations, two different imaging algorithms are used, plane wave imaging (PWI) and total focusing method (TFM). In PWI, a set of Q plane waves at Q different angles are emitted and the back-scattered signals at all elements are recorded, resulting in $Q \times N$ waveforms, where N is the number of activated elements transmitted and received[29]. In this research, the Q mentioned above is 1, all the elements of the phased array transducer emit incident waves at the same time and create a plane wave propagating to the longitudinal direction of the buffer plates. Because only one calculation of the wave propagation should be done for this simulation, the imaging analysis was possible in a short time.

The TFM functionality involves transmitting with each element of the transducer one by one and receiving at all the elements for each shot. A set of $N \times N$ signals is therefore recorded, where N is the number of activated elements transmitted and received[30].

Firstly, the defect imaging using the PWI without buffer ($L = 0$) were obtained using the calculated waveforms as shown in Fig. 3 (a). Then, the PWI imaging with a buffer of $L = 25$ mm was obtained as shown in Fig. 3 (b). The colors of the images represent intensities calculated by the PWI, normalized by the maximum intensity of each figure. The two defects inside the specimen can be clearly shown on the imaging area at the right positions. However, when the stacked plate buffer of $L = 25$ mm is used to connect the transducer and the specimen, the reflection from Defect 2 is distorted and can only be less clearly shown in the image. In this condition, the phased array transducer cannot perform as well as it directly

attached to the specimen. In addition, distinct spurious image behind the defect images were also obtained. To avoid the image distortion and the spurious images, the effective detecting region (EDR) is discussed in the next section.

3. The theoretical descriptions on the effective detecting region

Before analyzing the EDR, wave distortion by the dispersion nature of Lamb waves is discussed using the simple expression of the wave velocities of an S0 mode. We now assume that the incident wave from the vibration element is the pulse with the time width of Δt as shown in Fig. 4(a), and that its frequency spectrum has the bandwidth of Δf in the frequency range as in Fig. 4 (b). The maximum speed of $c_{\max}$ and minimum speed of $c_{\min}$ are found in the group velocity dispersion curve in Fig. 1 in the frequency range. Because the propagating velocities of the S0 mode varies with frequency, the waveform shown in Fig. 4 (a) can be distorted and spread as it propagates. After propagation at the distance of L in the plate, the pulse wave in Fig. 4 (a) is distorted and time duration of the wave at the propagation distance of L is ranging from $L/c_{\max}$ to $L/c_{\min} + \Delta t$ as shown in Fig. 4 (c).

Considering the imaging with PWI with the plate buffer, all the elements emit the signal with no delay and a plane wave is generated in the specimen. The echoes from a defect are individually received by each element. In this condition, it is natural to assume that the incident plane wave can propagate only the region extending straight out from the stack plate buffer. Assume that the distance between the surface of the specimen and the defect (or the position where the intensity value will be acquired in the image) is a, the farthest end of the buffer from the defect is b, the length of the buffer plate is L, as shown in Fig. 5, and the sound speed in the specimen is c. Figure 6 shows the waveforms at the two elements. (a) is at the element which is attached to the buffer plate at the nearest plate from the defect, and (b) is for the farthest plate from the defect. In the both cases, the reflected waves from the interface between the stacked plate buffer and the specimen which is one-round-trip echo and two-round-trip echo, respectively, are received at the same time. Between these two reflected waves the defect echo can be seen at the time different from the time the two reflected waves are received. The beginning time and ending time of these echoes are shown in these figures, following the simple representation of wave dispersion as shown in Fig. 4. To avoid the overlapping of the echo from defect and the reflected waves from the interface in Fig. 6 (a), the following equation should be satisfied,

$$2L/c_{min} + \Delta t < 2L/c_{max} + 2a/c \quad (1)$$

$$2L/c_{min} + 2a/c + \Delta t < 4L/c_{max} \quad (2)$$

Meanwhile, in Fig. 6 (b), the following equation should be satisfied,

$$2L/c_{min} + \Delta t < 2L/c_{max} + (a+b)/c \quad (3)$$

$$2L/c_{min} + (a+b)/c + \Delta t < 4L/c_{max} \quad (4)$$

The following set of equations can be founded after simplifying the equations (1)-(4),

$$2L/c_{min} + \Delta t < 2L/c_{max} + 2a/c \quad (5)$$

$$2L/c_{min} + (a+b)/c + \Delta t < 4L/c_{max} \quad (6)$$

Then, a and b can be expressed as,

$$a > c(L/c_{min} - L/c_{max} + \Delta t/2) \equiv a_0 \quad (7)$$

$$b < c(4L/c_{min} - 2L/c_{max} - \Delta t) - a \quad (8)$$

In the case of $a < b$, the equation (4) can be expressed as,

$$b < c(2L/c_{min} - L/c_{max} - \Delta t/2) \equiv b_0 \quad (9)$$

Summarizing Eqs. (7) and (9), the effective detecting region for PWI can be represented as the region surrounded by the red lines in Fig. 7.

In the case of TFM, the waveform emitted from a single element is reflected back and all elements receive the reflected waves. TFM can image not only the straight region extending from the buffer width, but also the region outside of it. Assuming that the distance between farthest plate from the defect is b and the closest plate from the defect is a, these are limited by the same equations as Eqs. (7) and (9). However, the definition of a is different from Eqs. (7) and (9), and the EDR is represented as in Fig. 9. It should be noted that the first reflections from the interface are not exactly the same in Fig. 6. If the incident and receiving elements are different, diffracted waves are expected to be measured instead of the first reflected wave in Fig. 6. Similarly, the two-round trips will also be slightly different, but we consider their effects to be small, and we have assumed here that it should be the same as in Eqs. (7) and (9).

4. Numerical analysis of the EDR for the imaging with a stacked plate buffer

To prove the simple theory of the EDR as described in the previous section, the calculations of the wave propagations and the imaging are conducted. For PWI, the positions of defects on the model are shown in Fig. 10 (a). The defects are set near the

boundaries of the EDR drawn in red contour. As shown in Fig. 10 (a), Defect 1 and 4 are located outside of the EDR with positions of (-12 mm, 11 mm), (3 mm, 33.5 mm), respectively, and Defect 2 and 3, with the positions of (-7 mm, 15 mm), (5 mm, 24 mm), respectively, are within the EDR. Figure 10 (b) is the imaging result with PWI. The colors of the images in this section also represent intensities calculated by each phased array algorithm, normalized by the maximum intensity of each figure. In the region between stacked plate buffer and the EDR contour, the high intensity image can be seen due to the large first reflection at the interface between the plate buffer and the specimen, which indicates the defects cannot be found in the PWI image in this region as predicted by the EDR. And also, as expected by EDR, Defect 1 and 4 are not visualized in the image and Defect 2and 3 can be found the image.

For TFM, the defects are set near the boundaries of the EDR drawn in red contour. As shown in Fig. 11 (a), Defect 1, 2, 3 and 4 are located outside of the EDR, with the positions of (0 mm, 35 mm), (-12 mm, 28 mm), (-20 mm, 20 mm), (-25 mm, 10 mm), respectively, while other defects, Defect 5, 6, 7 and 8, with the positions of (0 mm, 25 mm), (8 mm, 22 mm), (15 mm, 15 mm), (18 mm, 8 mm) are located within the EDR. The imaging result with TFM is shown in Fig. 11 (b). Different from the result in PWI, the high intensity image does not appear in the region between stacked plate buffer and the contour of the EDR, which indicates that the second reflected wave in the buffer is evaluated to be smaller in TFM than in PWI. In PWI, reflected waves with the same phase are repeatedly reflected back and forth in all plates, whereas in TFM, they are incident individually and the phases of these incident waveforms are not aligned in the calculation. Therefore, the round-trip waveform of the incident wave in the buffer is relatively larger in PWI. As a result, defects still can be found in this region using TFM. And as expected by EDR, Defect 1, 2, 3, and 4 are not visualized in the image, and Defect 5, 6 and 7 can be found in the image. However, Defect 8 cannot be seen in the image even though it is inside the EDR. This is the limitation of beam steering range in phased array transducers due to the directivity property[31].

According to the theoretical discussions in Sect. 3 and the result of the calculations of EDR, the stacked plate buffer is optimized here. From the equations shown in Sect. 3, it was derived that the EDR extends in proportion to the buffer length L. To solve the problem mentioned in Sect. 2 and in the calculations conducted in Sect. 4, imaging simulations with different buffer length L are done in this section for PWI and TFM. The results for L = 50 mm and 100 mm are shown in Figs. 12 and 13, respectively, which is double and quadruple of the previous length of buffer in Figs. 10 and 11. Figures 12 and 13 are for PWI and TFM,

respectively. The results of the defect imaging both by PWI and TFM show that the reflected waves from the interface between the stacked plate buffer and the specimen are removed from the imaging area when using the buffer with length of 100 mm as expected.

However, it should be noted that even though the influence from the interface between the stacked plate buffer and the specimen is removed from the imaging area by extending the length of the buffer, the distortion of the waveform of the Lamb wave propagating in the buffer plate due to the dispersion property is not considered. Ultrasonic attenuation due to the damping is not considered in these calculations, either. And there is the limitation of the buffer length due to the Lamb wave dispersion and the ultrasonic attenuation in the practical situation.

5. Conclusions

We proposed a stacked thin plate buffer to solve the problems when using phased array transducer to measure at high temperature. First, we describe the dispersion nature of the A0 and S0 mode Lamb wave at low *fd* range. From the properties of the S0 mode Lamb wave the size of the plates with thickness of 0.9 mm which make up the buffer are decided. Numerical calculations are applied, and the results showed the problem because of the reflection from the interface of the stacked plate buffer and the specimen. Second, the analysis of EDR is illustrated theoretically and show the limitation of the phased array transducer when attached with a stacked plate buffer. Numerical simulations of defect imaging with PWI and TFM agree well with the theoretical illustration. Based on the prediction from EDR, the spurious image of the second reflection from the interface between the buffer and specimen was removed by extending the buffer length.

Acknowledgments

This study was partially supported by the Japan Society for the Promotion of Science KAKENHI [Grant number 21H01573]

References

1) F. Endian, L. Yong, L. Xuewei, Surf. Topogr.: Metrol. Prop. **9** 025040 (2021).

2) S. Takaya, K. Miya, J. Mater. Process. Technol. **161**, 66–74 (2005).

3) A. Sugawara, K. Jinno, Y. Ohara, K. Yamanaka, Jpn. J. Appl. Phys. **54** 07HC08 (2015).

4) J. Kim, B. Lee, W. Hwang, S. Kang, Adv. Mater. Sci. Eng. **2015**, 1-8 (2015).

5) L. Yu, Y. Liu, H. Deng, S. Zhang, Y. Wang, Y. Zhou, IOP Conf. Ser.: Earth Environ. Sci. **859** 012012 (2021).

6) Y. Luo, W. Gu, W. Peng, Q. Jin, Q. Qin, C. Yi, Materials **13**, 2416 (2020).

7) S.H. Khodamorad, N. Alinezhad, D. H. Fatmehsari, K. Ghahtan, Case Stud. Eng. Fail. Anal. **5–6**, 59–66(2016).

8) Y. Ohara, S. Yamamoto, T. Mihara, K. Yamanaka, Jpn. J. Appl. Phys. **47**, 3908 (2008).

9) Y. Ohara, H. Nakajima, S. Haupert, T. Tsuji, T. Mihara, Jpn. J. Appl. Phys. **59**, SKKB01 (2020).

10) Y. Ohara, J. Potter, H. Nakajima, T. Tsuji, T. Mihara, Jpn. J. Appl. Phys. **58**, SGGB06 (2019).

11) R. I. Suleimanov, L. Z. Zainagalina, M. Y. Khabibullin, L. M. Zaripova, N. O. Kovalev, IOP Conf. Ser.: Mater. Sci. Eng. **327,** 032053 (2018).

12) I. Shin, S. Park, S. Kim, C. Seok, J. Koo, Int. J. Precis. Eng. Manuf. **16**, 65–71 (2015).

13) Y. Ohara, T. Oshiumi, H. Nakajima, K. Yamanaka, X. Wu, T. Uchimoto, T. Takagi, T. Tsuji, T. Mihara, *AIP Advances,* **7** (6): 065214 (2017).

14) R. Yan, C. Zhou, J. Phys.: Conf. Ser. **2610**, 012059 (2023).

15) Q. Li, Y. Chen, Y. Tang, H. Liu, J. Phys.: Conf. Ser. **2419**, 012071 (2023).

16) N. Xu, Z. Zhou, NDT E Int. **63**, 28–34 (2014).

17) J. Brizuelaa, J. Camachob, G. Cosarinskyc, J.M. Iriartec, J.F. Cruzab, NDT E Int. **101**, 1–16 (2019).

18) B. Zhang, D. Liu, F. Shi, H. Dong, Chinese Phys. B. **22**, 014302 (2013).

19) H. Sui, P. Xu, J. Huang, H. Zhu, Sensors **21**, 55 (2021).

20) Y. Dai, S. Yan, B. Zhang, Chinese Phys. B **30**, 074301 (2021).

21) Y. Ohara, T. J. Ulrich, M. C. Remillieux, K. Tsunoda, T. Yamada, T. Tsuji. T. Mihara. Jpn. J. Appl. Phys. **62**, SJ1019 (2023).

22) H. Wu, J. Chen, K. Yang, X. Hu, Meas. Sci. Technol **2**, 045401 (2016).

23) T. Ihara, N. Tsuzuki, H. Kikura, Prog. Nucl. Energy **82**, 176-183 (2015).

24) F. M. Foudzi, I. Ihara, J. Phys.: Conf. Ser. **520**, 012025 (2014).

25) E. Abbe, J. R. Microsc. Soc. **3**, 790–812 (1883).

26) A. A. Maznev, O. B. Wright, Wave Motion **68**, 182-189 (2017).

27) T. Fukuchi, T. Hayashi, N. Mori, Jpn. J. Appl. Phys. **62**, SJ1005 (2023).

28) M. Xia, T. Hayashi, and N. Mori, Proc. of Symp. on Ultrasonics Electronics, (USE2023) 44, 2E3-1.

29) L. L. Jeune, S. Robert, E. L. Villaverde, C. Prada, Ultrasonics **64**, 128-138 (2016).

30) C. Holmes, B. W. Drinkwater, P. D. Wilcox, NDT E Int. **38**, 701–711 (2005).

31) Sumana, A. Kumar, NDT E Int. **116**, 102324 (2020).

Figure Captions

Fig. 1. (Color online) Group velocity dispersion curve of Lamb wave in the low *fd* range.

Fig. 2. (Color online) Geometries of the calculation model.

Fig. 3. (Color online) Defect imaging with and without a stacked plate buffer.

Fig. 4. (Color online) Schematic to show the distortion of incident pulse propagating in a thin plate.

Fig. 5. (Color online): Model to show the effective detecting region for PWI.

Fig. 6. (Color online) Typical waveforms at the two elements, one is the element attached to the plate nearest from the defect, and the other is the element attached to the plate farthest from the defect when PWI is used.

Fig. 7. (Color online): The effective detecting region (EDR) for PWI.

Fig. 8. (Color online): Model to show the effective detecting region for TFM.

Fig. 9. (Color online) The effective detecting region in TFM.

Fig. 10. (Color online): Calculation model and result for PWI with a stacked plate buffer.

Fig. 11. (Color online): Calculation model and result for TFM with a stacked plate buffer.

Fig. 12. (Color online): PWI images with a stacked plate buffer with different length.

Fig. 13. (Color online): TFM images with a stacked plate buffer with different length.

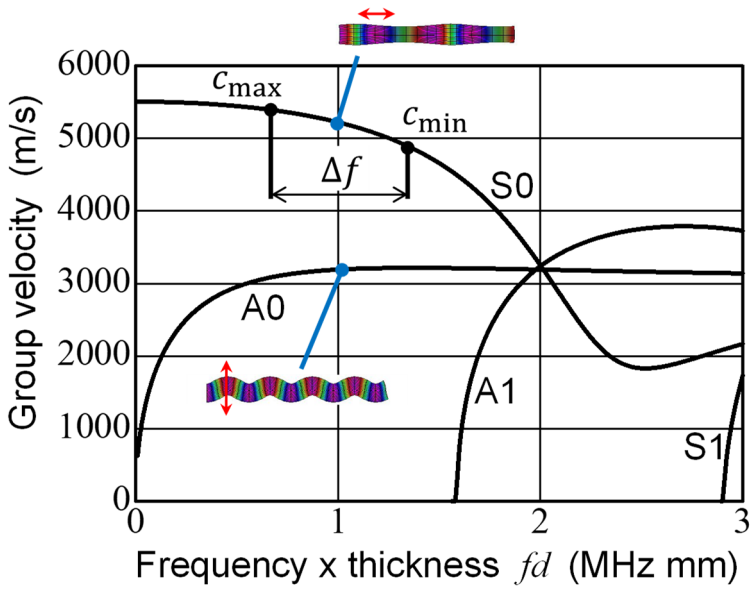

Fig. 1. (Color online) Group velocity dispersion curve of Lamb wave in the low *fd* range.

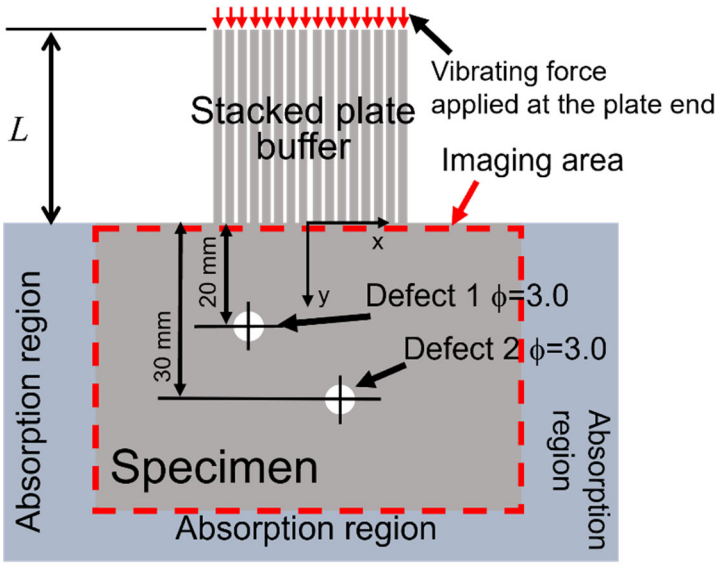

Fig. 2. (Color online) Geometries of the calculation model.

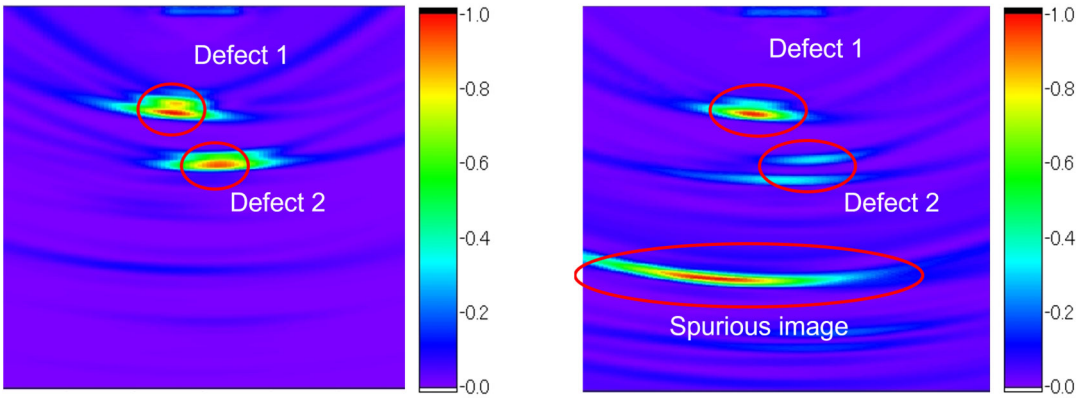

(a)No buffer (b)Using a buffer of L = 25mm

Fig. 3. (Color online) Defect imaging with and without a stacked plate buffer.

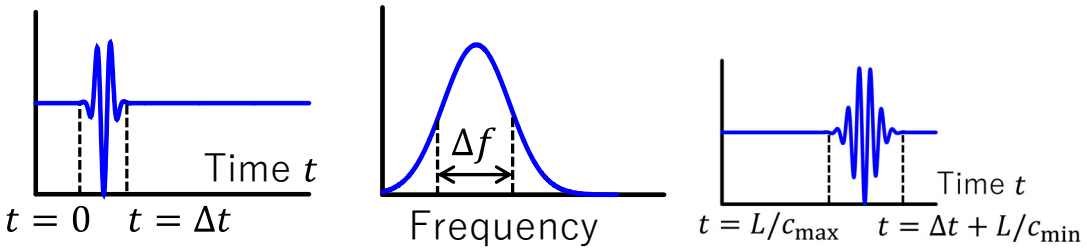

(a) Incident pulse (b) Frequency spectrum of (a) (c) Waveform at the plate end

Fig. 4. (Color online) Schematic to show the distortion of incident pulse propagating in a thin plate.

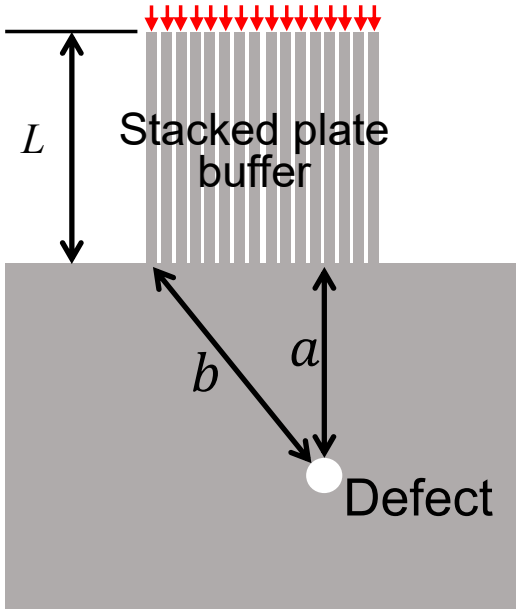

Fig. 5. (Color online) Model to show the effective detecting region for PWI.

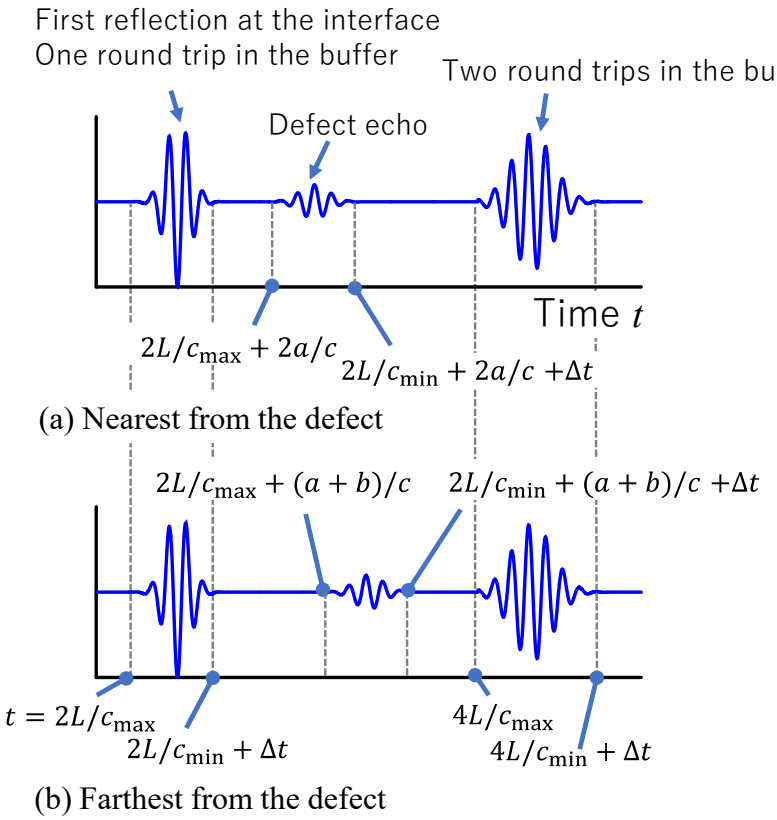

Fig. 6. (Color online) Typical waveforms at the two elements, one is the element attached to the plate nearest from the defect, and the other is the element attached to the plate farthest from the defect when PWI is used.

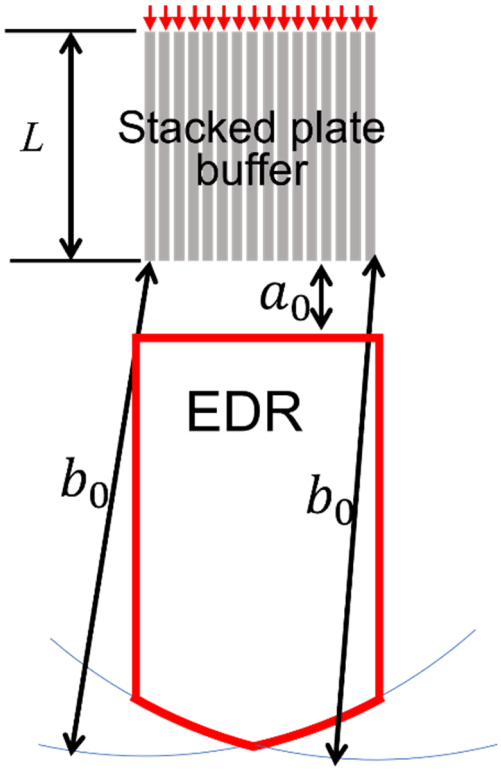

Fig. 7. (Color online) The effective detecting region (EDR) for PWI.

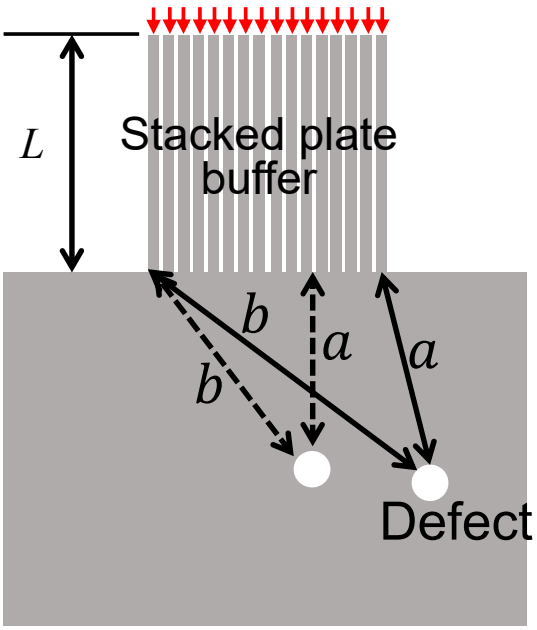

Fig. 8. (Color online) Model to show the effective detecting region for TFM.

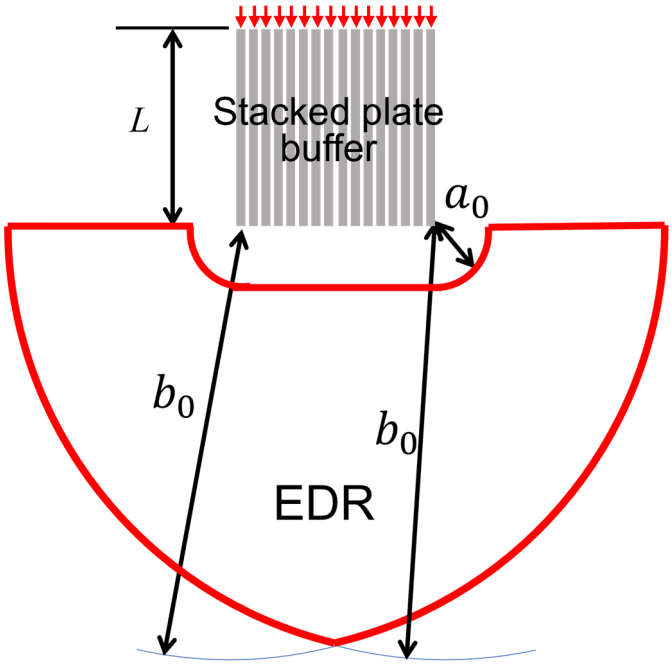

Fig. 9. (Color online) The effective detecting region in TFM.

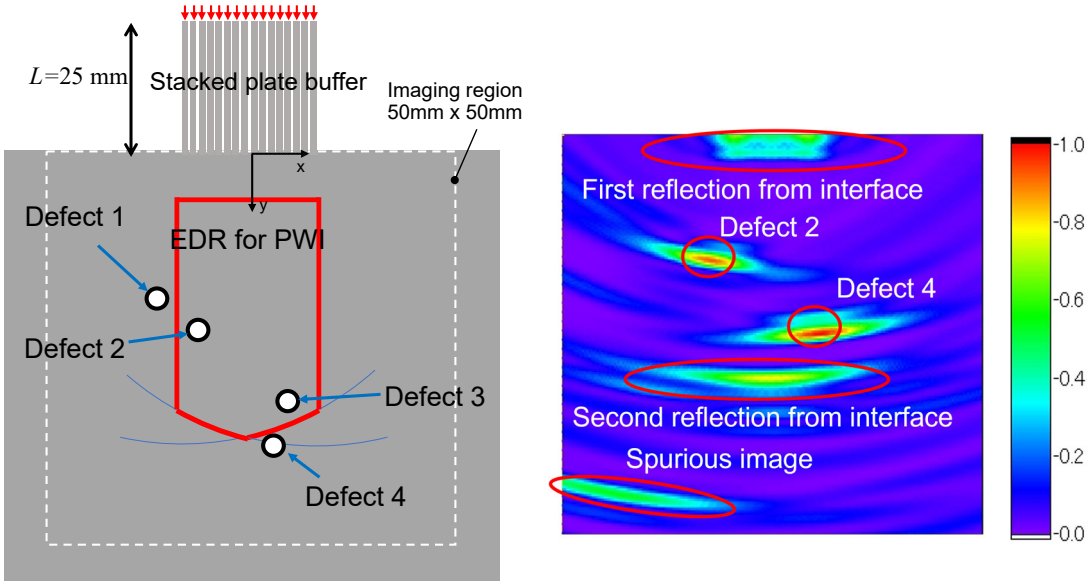

(a) Geometries of the calculation model

(b) Image with a stacked plate buffer of L= 25 mm

Fig. 10. (Color online) Calculation model and result for PWI with a stacked plate buffer.

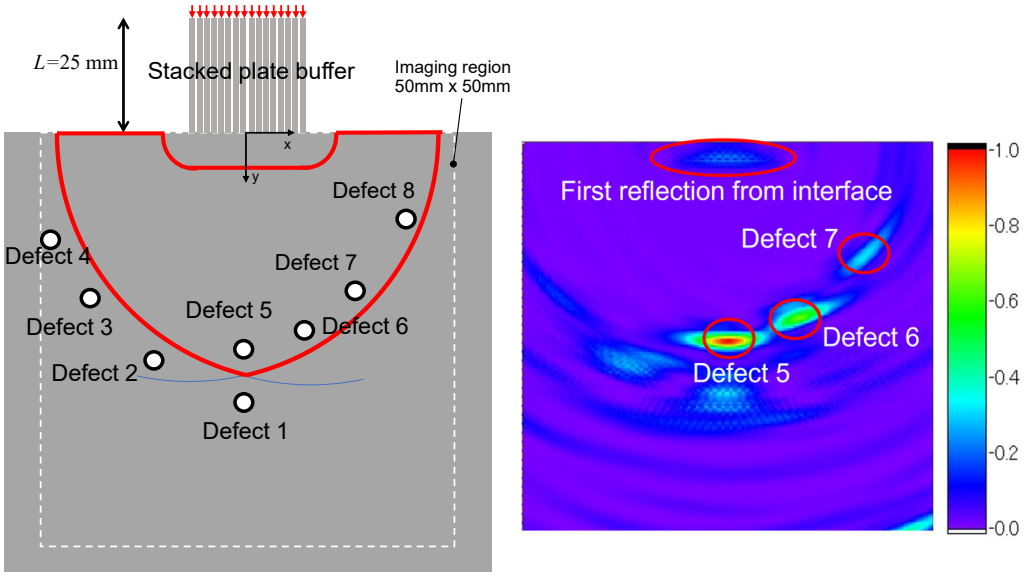

(a) Geometries of the calculation model (b) Image with a stacked plate buffer of L= 25 mm

Fig. 11. (Color online) Calculation model and result for TFM with a stacked plate buffer.

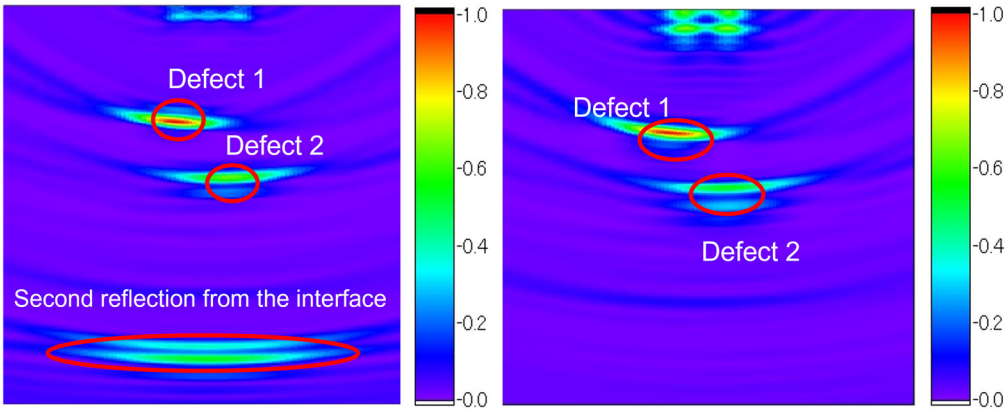

(a) L = 50 mm (b) L = 100 mm

Fig. 12. (Color online) PWI images with a stacked plate buffer with different length.

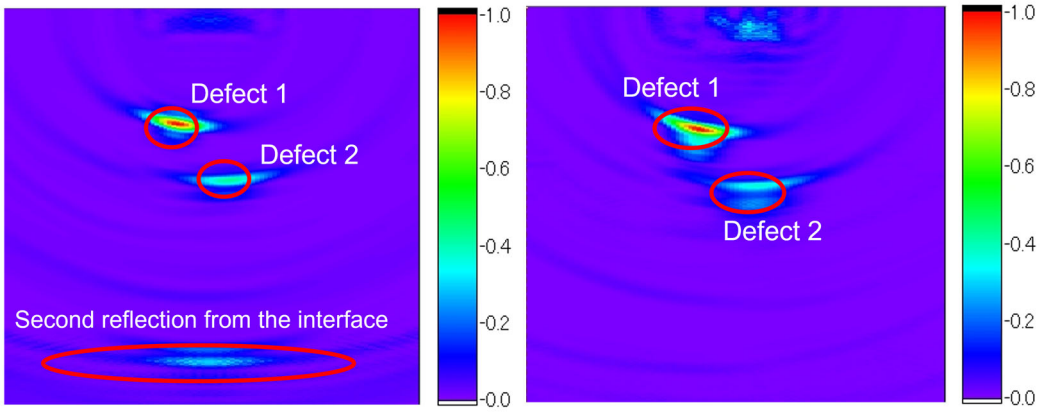

(a) L = 50 mm (b) L = 100 mm

Fig. 13. (Color online) TFM images with a stacked plate buffer with different length.